Tetrahedral framework of inverse opal photonic crystals defines the optical response and photonic band gap

Alex Lonergan[1], David McNulty[1] and Colm O'Dwyer[1,2,3*]

[1]*School of Chemistry, University College Cork, Cork T12 YN60, Ireland*
[2]*Micro-Nano Systems Centre, Tyndall National Institute, Lee Maltings, Cork T12 R5CP, Ireland*
[3]*Environmental Research Institute, University College Cork, Lee Road, Cork T23 XE10, Ireland*

Abstract

By forming anatase TiO_2 inverse opals by infiltration of an opal photonic crystal, we demonstrate that the optical response and angle-resolved blue-shift of the band-gap of the inverse opal structure is defined by a particular three-dimensional structure of the infilled voids. The optical structure of TiO_2 inverse opals usually displays significant deviation from its physical structure and from theoretically predicted position of the photonic band-gap. Following rigorous structural characterization of the parent opal template and TiO_2 inverse opals, alternative explanations for the signature of optical transmission through inverse opals is proposed. These approaches posit that, for light-matter interaction, an inverse opal is not precisely the inverse of an opal. Accurate parameters for the structure and material properties can be obtained by invoking a Bragg FCC selection rule-forbidden (-211) plane, which is not a realistic model for diffraction in the IO. Alternatively, by assuming optical interactions with just the periodic arrangement of tetrahedral filled interstitial sites in the structure of inverse opal, a complete reconciliation with spectral blue-shift with angle, photonic band gap and material parameters are obtained when a reduced unit cell is defined based on interstitial void filling. The analysis suggests a reduced interplanar spacing ($d = 1/\sqrt{3}\ D$, for pore diameter D), based on the actual structure of an inverse opal in general, rather than a definition based on the inverse of an FCC packed opal. This approach provides an accurate and general description for predicting the spectral response and material parameters of ordered inverse opal photonic crystal materials.

I. INTRODUCTION

Nanostructured photonic crystal materials are among the most widely studied materials in recent years with promising applications in photonics and optoelectronics. Photonic crystals in particular, feature a periodic dielectric material which can be tuned to inhibit light propagation in certain directions[1,2], and these periodically porous material systems and their ability to reflect, diffract and guide photons have been applied to a plethora of physical and chemical technologies. More recently, programming 3D structure into inorganic materials chosen for a particular use has proven the effectiveness of having an interconnected ordered porous structure. Mapping their optical properties in real-time provides opportunities to track changes to materials under certain conditions in a host of applications[3], by visible spectroscopy that exploits the unique band structure that ordered porous materials exhibit. Knowing the exact structure is paramount to defining and understanding how it interacts with light, and it is clear that there are some inconsistencies in the literature regarding the true structure of the inverse replica of an opal photonic crystal.

In a PhC, the range of inhibited frequencies is known as the photonic band gap (PBG) of the photonic crystal. A pseudo-photonic band gap (p-PBG) is also possible in dielectric materials of lower dielectric contrast, in which there is significant yet incomplete depletion of the inhibited frequency range. These p-PBGs are typically reported features of artificial opal templates, such as ordered polystyrene or PMMA sphere templates[4]. Of particular interest are inverted opal materials with high dielectric contrast and a tuneable PBG[5], presenting many opportunities in optical[6,7], energy storage[8-10] and biological fields[11,12]. Theoretical approaches to modelling a true PBG for an inverse opal material suggest a need for a high dielectric contrast of $n \geq 2.8$[13]. TiO_2 is a well-documented and attractive material as an inverse opal candidate due to its low cost, facile synthesis, chemical stability[14] and photochemical applications[15]. It is also an excellent candidate for achieving a true optical PBG with reported high refractive indices of up to 2.74[16], depending on the phase of the material.

Inverse opal materials are commonly prepared via infiltration of an ordered opal template, leaving the structure of the inverse opal largely dependent on the initial opal structure[17]. Consequently, order in the opal template is of a paramount importance to the quality of inverse opal replication. Order in the opal template is largely controlled by the chosen method of deposition. Sphere coatings can be obtained through several different methods; drop-casting[18], spin coating[19], dip coating[20], electrophoretic deposition[21] and

Langmuir-Blodgett[22] type approaches. High quality templates, reproducibility and relative simplicity of the dip-coating technique make it an attractive option in preparing opal templates. Dip coating of the sphere template has been shown to produce ordered multi-layer deposits of spheres across a wide area of the sample template[23], ideal for creating long range order for optical analysis. Additionally, the thickness, coverage and number of layers of the deposited opal film can be controlled by varying surface hydrophilicity, temperature, humidity, withdrawal speed and contact angle with the suspension[24].

Opal-based photonic crystals have been extensively examined as a model system for controlling the flow of light[25], and form a basis for optical waveguiding[26], enhanced angle-dependent absorbers for tandem solar cells[27], as sensors[28], photocatalytic materials[29] and more recently as templates for Li-ion battery material[30-32]. The periodic framework and presence of a PBG in photonic crystal structures has led to their increased interest as lasing media, with reports of enhanced light confinement[33] and an improved lasing threshold[34] arising from inverse opal based gain media. Photonic crystals are also attractive materials in the field of nonlinear optics with reports of drastically improved second[35,36] and third[37,38] harmonic generation from periodic dielectric structures, achieved through tuning the pump wavelength with respect to the position of the PBG. Structural properties such as material size and layer composition, in addition to inherent material properties including effective refractive indices and their modification by changes to order, index contrast by chemical modification of the phase, swelling effects, or even slower group velocity photons for enhancing photochemistry can be probed from opal and inverse opal photonic crystal-based structures. Accurately defining the PBG for inverse opals is critical for understanding, tracking or mapping fundamental changes in photonic crystal architectures, such as material phase or state of charge in electrochemical settings[8]. Calcined inverse opal structures have proven to be more complex to make, but also to interpret, with discrepancies often arising between the theoretical and experimental observations[39]·[40]. Calcined inverse opal structures represent a direct inversion of the infiltrated opal template with air spheres surrounding an interconnected scaffold of crystalline material. Inverse opal materials prepared from alternative methods, such as those produced from atomic layer deposition, report strong correlation between experimental results and theoretical predictions[41,42]. These types of inverse opal materials may be better described as shells of crystalline material arranged as an opal, and differ slightly in composition from direct inverted opal materials.

Here, we uncover the particular structure of an inverse opal that accurately explains their optical transmission spectra. We also show that, generally, the optics of an inverse opal is not the inverse of an opal. By rigorous physical and optical characterization of dip coated polystyrene micro-sphere opals, alongside their corresponding TiO_2 inverse opals, our data demonstrate that the periodic structure formed by infilling of an opal, is distinctly different to a refractive index-flipped inverse of an opal. The FCC packed structure and analysis based on the standard interplanar spacing of the Bragg-Snell model, is not an accurate approach to quantifying the nature of the inverse opal spectrum. Specifically, sphere sizes, refractive indices and pore sizes are accurate when the periodic structure is no longer related to the parent opal FCC lattice, and defined according to the 3D interconnected structure of tetrahedral vacancies of the opal that are infilled. In this case, accurate parameters for the inverse opal are possible, and we posit this as a general approach to accurately describe the transmission spectra for any inverse opal, and in the process help to reconcile the differences between the true structure of the inverse opal, and incorrect values predicted from Bragg-Snell analysis of transmission spectra for periodically porous materials.

II. EXPERIMENTAL METHOD

Materials and substrate preparation

350 and 500 nm diameter polystyrene spheres in 2.5 wt% aqueous suspension with minimal added surfactant, were purchased from Polysciences Inc. Polystyrene sphere particles contained a slight anionic charge from the sulphate ester used in formation, giving the sphere suspension a negative charge. All sphere suspensions were used as received. Sodalime glass coated with a conductive layer of fluorine-doped tin oxide (FTO), purchased from Solaronix SA, was used as the substrate for colloidal crystal formation. Substrates of thickness 2.2 mm, were cut into pieces of sizes 10 mm × 25 mm. Prior to colloidal crystal formation, all samples were sonicated in acetone (reagent grade 99.5%; Sigma-Aldrich), followed by sonication in isopropyl alcohol (reagent grade 99.5%; Sigma-Aldrich) and finally sonicated in deionized water. Samples were dried in an inert atmosphere at room temperature. Effective substrate coating areas, of approximate sizes 10 mm × 10 mm, were created by applying Kapton tape to the remainder of the substrate area, both front and back. Covering the back of the sample also ensured that the colloidal crystal template would form on the conductive layer as

desired. Finally, all substrates were treated in a Novascan PSD Pro Series digital UV-Ozone system for one hour prior to the coating process, so as to improve surface hydrophilicity of the substrate[43].

Colloidal crystal template and TiO_2 inverse opal formation

Immediately following UV-Ozone treatment, the substrates were immersed in pre-heated vials of a suspension of as-received PS spheres and dip-coated following withdrawal at a rate of 1 mm min^{-1}. Short cylindrical vials of ~16 mm diameter were used to minimize the quantity of sphere suspension (1.5 – 2.0 mL). Sphere suspensions were gently heated to temperatures of ~40 – 50°C prior to use, to improve the quality and thickness control of the coating. Substrates were also tilted at a slight angle (10 – 20°) from the vertical upon immersion to improve adhesion to the substrate [24]. The substrate was allowed to remain in the suspension for another 10 minutes, so as to allow time for the suspension to settle to a minimum energy state from surfactant-mediated repulsion. The relatively fast withdrawal rate of 1 mm/min minimizes the formation of bands or streaks in the coated template. Coated templates were allowed to dry in an inert atmosphere at room temperature.

TiO_2 inverse opals were formed via infiltration of a polystyrene sphere template with a $TiCl_4$ precursor followed by calcination at 450°C in air for 1 h to oxidize and crystallize the material. The $TiCl_4$ complex used was a 0.1 M solution of titanium(IV) chloride tetrahydrofuran complex ($TiCl_4 \cdot 2THF$, 97 %; Sigma-Aldrich).

Structural and optical characterisation

SEM analysis was carried out using a Zeiss Supra 40 high resolution SEM at an accelerating voltage of 10 kV. Raman scattering analysis was carried out using a Renishaw InVia Raman Spectrometer with a 30 mW Ar^+ laser at 514 nm excitation. The beam was focused using a 40x objective lens and collected using a RenCam CCD camera. Optical transmission analysis was performed using a quartz tungsten-halogen lamp operating from 400 - 2200 nm from Thorlabs Inc., a UV-Visible spectrometer (USB2000+ VIS-NIR-ES) with operational range 350 – 1000 nm from Ocean Optics Inc. and a NIR spectrometer (NIRQuest512-2.5) with operational range 900 – 2500 nm, also from Ocean Optics Inc. A motorised rotation stage (ELL8; Thor Labs Inc.) was used to vary the incidence angle in transmission measurements.

III. RESULTS AND DISCUSSION

Inverse opals of TiO_2 from colloidal photonic crystals

To uncover the structure of the inverse opal photonic crystal that affects angle-resolved optical transmission, we first detail the structure and optical response of the parent opal colloidal crystal. While the optical properties resulting from a pseudo photonic band gap are well known for 3D opals, it is important nonetheless to confidently compare the behaviour of the opal template from which inverse opal TiO_2 is formed, so that the inconsistency in the Bragg-Snell approach for the inverse opal structure are shown and defined from a consistent overall synthetic protocol. SEM images of colloidal crystal of polystyrene (PS) spheres and the corresponding TiO_2 inverse opals (IOs) are shown in Figure 1. Also shown are the corresponding size distribution analyses for the sphere diameter in each opal, and the pore diameter in the corresponding IOs. All SEM images were taken from opals and IOs prepared on fluorine-doped tin oxide (FTO) coated glass in order to provide a conductive layer for scanning electron microscopy. The statistical distribution of dimensions in Figs 1(e-h) (see Supplementary Materials Fig. S2 for further details) are consistent with quoted diameters of the as-received PS spheres i.e. 350 nm (measured as 342 ± 11 nm) and 500 nm (measured as 492 ± 22 nm) for spheres shown in Fig. 1 (a) and (b), respectively.

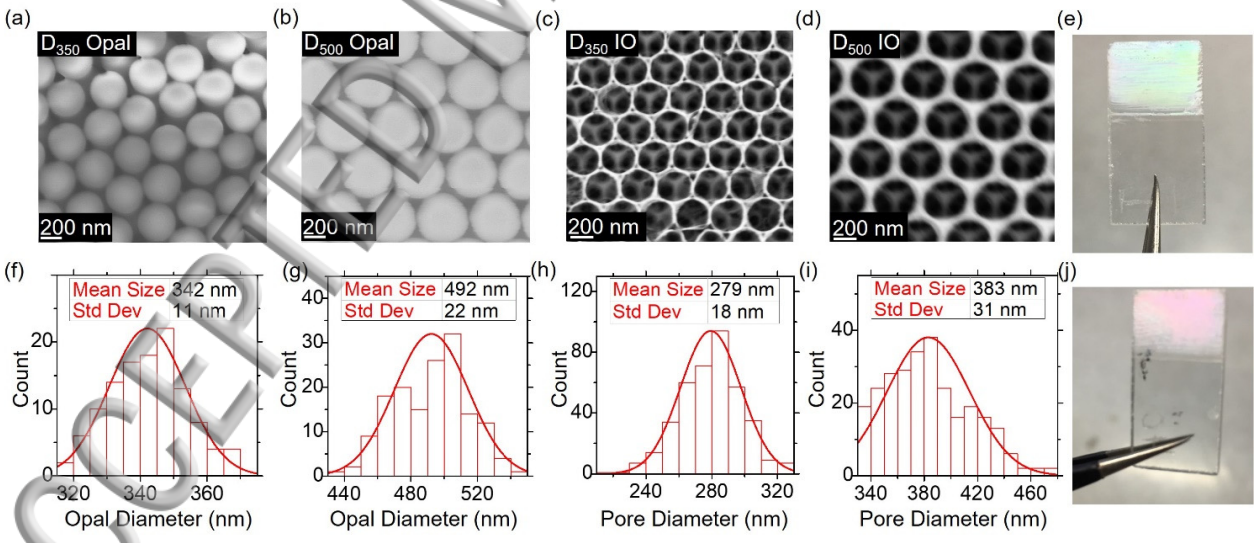

Figure 1. SEM images of PS spheres (a) 350 nm, (b) 500 nm, (c) SEM images for TiO_2 IOs from PS sphere templates of size 350 nm and (d) 500 nm. Size distribution analyses for (f) 350 nm PS spheres, (g) 500 nm PS spheres, (h) 350 nm TiO_2 IO and (i) 500 nm TiO_2 IO. Optical images of prepared (e) 350 nm and (j) 500 nm TiO_2 IO samples.

The SEM images for the PS spheres, show a uniform, ordered surface, displaying the typical FCC ordered arrangement typical of a self-assembled colloidal crystal or opal[44-47]. The relatively narrow

standard deviation range confirms a high degree of order within the colloidal crystal, which was translated to the inverse structure upon infilling and thermal decomposition of the opal template. In the case of the TiO_2 IOs, Fig. 1 (c) and (d) display SEM images confirming the expected inverse opal geometry, with subsequent layers visible underneath the top layer in the typical FCC layered fashion. The number of layers of material was estimated from SEM images, with approximately ten layers present in each case (see Supplementary Materials Fig. S1 for accompanying SEM image). The TiO_2 IO was found to achieve good coverage of the sample substrate. The IO template can be seen to feature several cracks across the surface, with large domains or islands of IO material formed. Typical IO domains are approximately 40 × 90 μm in size (see Supplementary Materials Fig. S1 for larger images of IO morphology). Statistical analysis of the IO dimensions confirms that for IOs the mean pore diameter reduces in size compared to the parent opal sphere diameter. This shrinkage upon inversion is a well-documented feature of inverted opal materials, commonly attributed to the calcination and volume filling from increased molar volume of TiO_2 as a solid[42,48]. In our case, detailed characterization of the IO from a colloidal route to high quality IOs, is important for interpretation of their spectroscopic signature. In this instance, the measured 342 nm PS spheres render a mean IO pore size of 279 nm (18% reduction), while the measured 492 nm PS spheres as an FCC opal, have been reduced to a mean IO pore size of 383 nm (22% reduction). Calculated standard deviations from the mean pore size (18 nm for the 279 nm IO and 31 nm for the 383 nm IO) suggest a typical IO pore size that is ~80% of the parent opal sphere diameter. Note, our analysis also confirms that the reduction is consistent across the IO (see Supplementary Materials).

To ascertain the phase consistency of TiO_2 present in the IOs, Raman scattering analysis was carried out on all samples used in this study. Knowledge of the phase of TiO_2 becomes important for an accurate determination of the refractive index of the material. TiO_2 can crystallize in three different phases [49,50], with each phase reported as having a different refractive index[51]. Figure 2 (a) shows the collected Raman spectra for TiO_2 IOs prepared from 500 nm (D_{500}) and 350 nm (D_{350}) diameter PS sphere opals. Each spectrum displays four distinct peaks at approximately 152, 401, 524 and 643 cm^{-1}, corresponding to the E_g, B_{1g}, A_{1g} and E_g phonon modes of TiO_2, respectively [52], confirming uniquely anatase phase for all TiO_2 IOs.

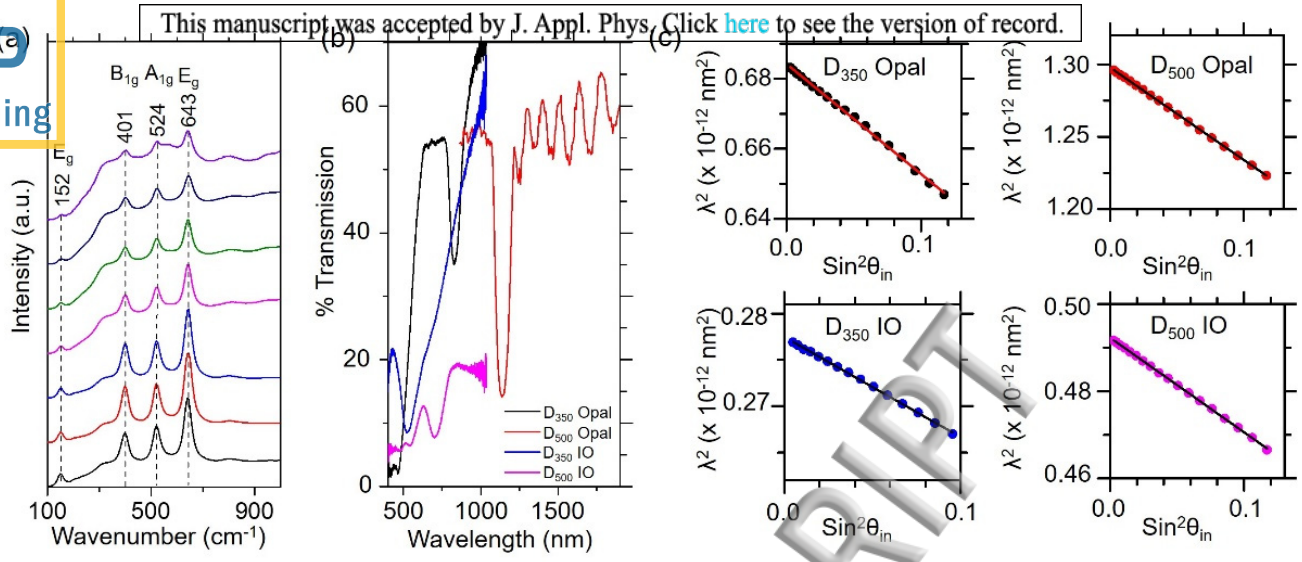

Figure 2. (a) Raman scattering spectra for TiO_2 IOs prepared on FTO coated glass, (b) Optical transmission spectra for opals formed using D = 350 and 500 nm PS spheres. Spectra from their corresponding IOs are also shown. (c) Bragg-Snell plots obtained from angle-resolved transmission spectra recorded at 1° intervals for D = 350 and D = 500 nm opals, and also from their corresponding IOs.

Figure 2 (b) shows the optical transmission spectra collected for D_{350} and D_{500} PS spheres and their corresponding TiO_2 IO. All transmission data shown was collected at 0° to the incident light source. The D_{350} PS opals, D_{350} IO and D_{500} IO were examined in the wavelength range 400 – 1000 nm, whereas the D_{500} PS opals were examined between 850 – 1900 nm where the expected band gap appears. The primary transmission dips (including the photonic band gap) associated with angle-resolved diffraction from the FCC ordered lattice of PS opals are in excellent agreement with the theoretical predictions from the Bragg-Snell model:

$$\lambda_{hkl} = \frac{2d_{hkl}}{m}\sqrt{{n_{eff}}^2 - sin^2\theta} \qquad (1)$$

For an FCC (111) plane, d_{111} is equivalent to 0.816 D, where D is diameter of the PS sphere or IO pore diameter. One of the more commonly applied models for approximating an effective refractive index is the Drude model[53-56] for a two material system:

$$n_{eff} = \sqrt{n_1^2\,\varphi_1 + n_2^2\,\varphi_2} \qquad (2)$$

In accordance with the Bragg-Snell law (Eqn 1) and (Eqn 2), assuming a first order resonance of m = 1, polystyrene (n = 1.59 – 1.60[57]) and air (n = 1) in an FCC geometry gives an effective refractive index of n_{opal} = 1.46, with a predicted (111) transmission dip (band gap) of 1172 nm for 492 nm (D_{500}) PS spheres and

815 nm for 342 nm (D_{350}) PS spheres. Experimentally, the corresponding transmission dips were observed at 1142 nm and 832 nm respectively. However, for the TiO_2 IO materials, the expected transmission dips for the FCC (111) plane are not observed. Anatase TiO_2 (n = 2.49)[51] and air (n = 1) in an FCC geometry yield an effective refractive index of n_{IO} = 1.53 giving a predicted (111) transmission dip of 959 nm for 383 nm TiO_2 pore diameters and 699 nm for 279 nm TiO_2 pore diameters. These predictions differ drastically from experimental observations for the corresponding IO structures, where transmission dips were observed at 703 nm and 528 nm respectively. A large discrepancy exists between the theoretical and experimental observations in the case of the inverted opal structure, with other works also reporting a deviation from expected PBG positions for IO materials[39,40], without explicit identification of the cause. However, experimentally observed PBGs are in excellent agreement with the observed structural colour of each IO sample, as seen in Fig. 1 (e) and (j).

From angle-resolved transmission spectra, data are presented in Fig. 2 (c) in accordance with the Bragg-Snell relation:

$$\lambda_{hkl}^2 = \frac{4d_{hkl}^2}{m^2} {n_{eff}}^2 - \frac{4d_{hkl}^2}{m^2} sin^2\theta \qquad (3)$$

This can be said for both the PS opals and the TiO_2 inverse opals, in spite of the significant blue shift in the band gaps for IOs compared to theoretical predictions. The reader is referred to Supplementary Materials Fig. S4 and associated description for further details.

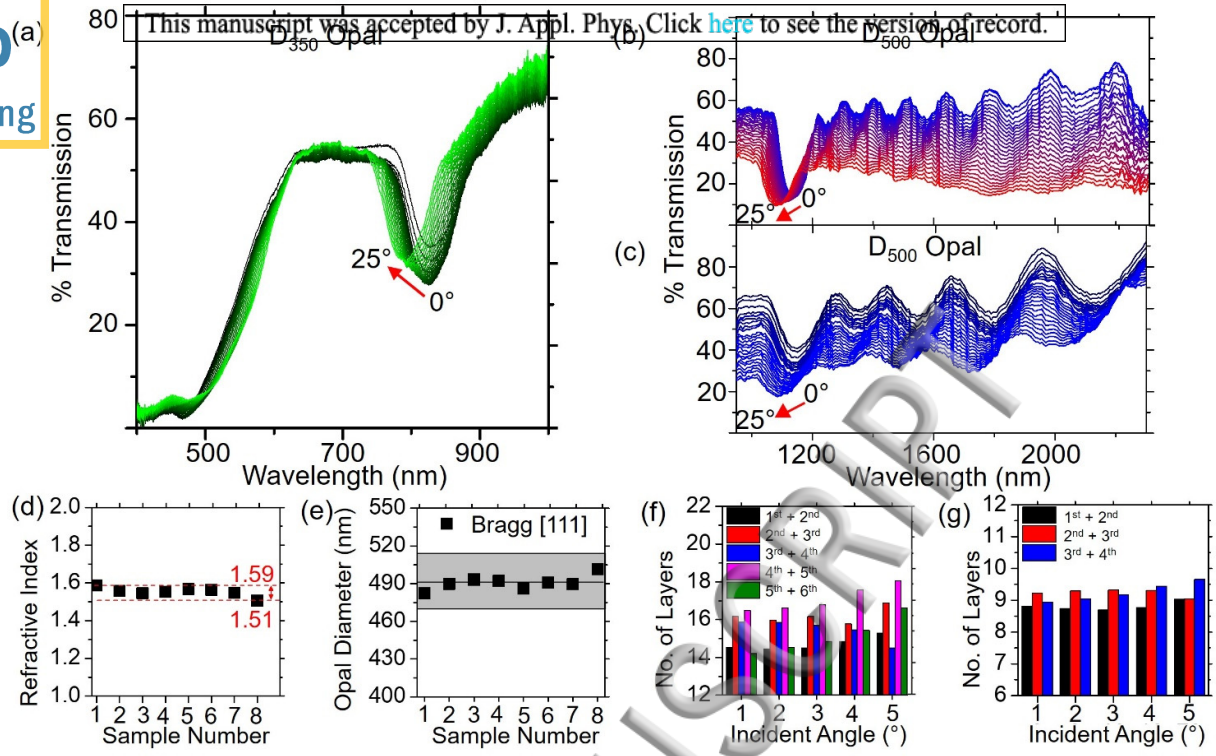

Figure 3. (a) Optical transmission spectra for D_{350} PS opals. (b), (c) Optical transmission spectra for D_{500} PS opals. (d) Bragg-Snell calculated PS refractive indices. (e) PS sphere diameter estimated from Bragg-Snell analysis of transmission spectra. The shaded grey region represents one standard deviation about the SEM measured mean shown in Fig. 1 (g). All transmission minima were assumed to be resultant from a (111) plane interaction with $d_{hkl} = \sqrt{(2/3)}\ D$. (f), (g) Fabry-Perot analysis for D_{500} PS opals. Bare FTO coated glass is normalized to 100% transmission.

The gradual angle-dependent shift in the transmission minima and Fabry-Pérot resonances in Fig. 3 (a) for the D_{350} opal and Fig. 3 (b,c) for the D_{500} opal between 0 and 25° maintains a consistent spectral shape. For the D_{500} opal, the (111) plane of the fcc lattice opens up the PBG and a transmission minimum at ~1140 nm. However, at longer wavelengths, a series of Fabry-Pérot resonances are observed[58], indicative of high quality and long range order in the opal template[59]. As the nature of the PBG of the inverse opal TiO_2 depends on the quality of the colloidal crystallization of the parent opal, we estimated the consistency in optical quality of both D_{500} and D_{350} opals. In Fig. 3 (b) and (c), the number of Fabry-Perot resonances changes from six to four, respectively, for two different samples coated with identical D_{500} PS opals. The differences arise from the thickness of the opal coating, which is related to many factors in dip-coating process including; the surface hydrophilicity, tilt angle, temperature, humidity and the presence of a surfactant[24]. For an opal coating of height, h, and two adjacent Fabry-Perot minima, λ_i and λ_{i+1} ($\lambda_i < \lambda_{i+1}$), the height of the structure can be calculated[60] from:

$$h = \frac{\lambda_i}{2n_{eff}\cos\theta\left(1-\frac{\lambda_i}{\lambda_{i+1}}\right)} \quad (4)$$

From the height of the sphere stack, we estimated the number of layers present. For a total of N layers of spheres of diameter D, in an FCC stacking sequence of height, h, the height is:

$$h = D + (N-1)\frac{\sqrt{3}}{2}D \quad (5)$$

From Eqn 4 and Eqn 5, an estimate of the number of stacked 2D layers comprising the 3D IO are shown in Fig. 3 (g) and (h). For the spectrum shown in Fig. 3 (b) with six visible Fabry-Perot oscillations, the data estimate ~16 layers or ~9 layers (Fig. 3(c)) of PS spheres. Fig. 3 (e) and (f) display the results of Bragg-Snell analysis (as per Eqn 3) carried out on eight different D_{500} opals, showing the calculated refractive index of PS, and correlation to the sphere diameter, respectively. The refractive index data is consistent between each of the opals we examined, ranging from 1.51 – 1.59, comparing favourably with the quoted values for PS (n = 1.59-1.60[57]). All opal diameters, calculated experimentally from Eqn 3, fall within one standard deviation of the mean, with many being close to the actual mean (solid black line). The reproducibility and consistency of these results confirms the long-range order in the 3D opal colloidal photonic crystal structure as templates to form ordered inverse opals.

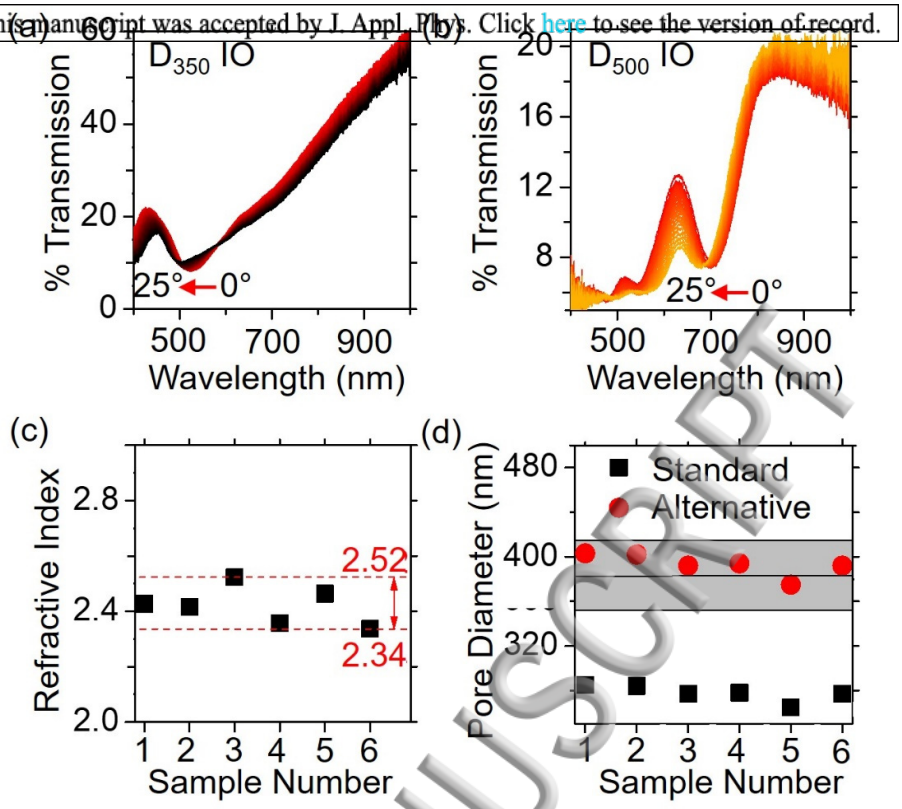

Figure 4. Optical transmission spectra for (a) D_{350} and (b) D_{500} TiO_2 inverse opals. (c) Bragg-Snell calculations for TiO_2 refractive indices based on PBG shift. (d) Inverse opal pore diameters calculated from the standard $d_{hkl} = \sqrt{(2/3)}$ D and proposed alternative $d_{hkl} = 1/\sqrt{3}$ D unit cell approach. The shaded grey region represents one standard deviation about the SEM measured mean shown in Fig. 1 (i).

The inverse opal structure based on interstitial void filling

Next, we detail the spectral response of a TiO_2 inverse opal made from the opal photonic crystals described above in Fig. 1, and elucidate an alternative interpretation that correctly explains the optical transmission spectra and PBG of an IO in general. The optical transmission spectra for TiO_2 inverse opals grown from parent D_{350} and D_{500} opals are shown in Fig. 4 (a) and (b), respectively. As per Eqn 1, the position of the transmission minimum band gap blue-shifts slightly with a widening in the angle of incidence. In comparison with the PS opal spectra, the corresponding TiO_2 IOs cause notable scattering, consistent with a porous or polycrystalline film[61]. Calculated refractive index and pore diameter data from Eqn 3 are shown in Fig. 4 (c) and (d) for six different TiO_2 IOs prepared from D_{500} PS opal templates, respectively. From Fig. 4 (c), the range of calculated refractive indices for TiO_2 from Eqn 2 vary from 2.34 to 2.52. This range compares favourably to literature values for anatase TiO_2 (n ~ 2.49). Effective refractive indices were

calculated from Eqn 3, independently of the calculated pore diameter. From a typical Bragg-Snell plot, as in Eqn 3, the slope is -4 d_{hkl}^2 with an intercept of 4 d_{hkl}^2 n_{eff}^2, and the ratio of these values gives the effective refractive index (n_{eff}) of the material, without any need to ascertain the true value for d_{hkl} and hence the IO pore diameter *D*. While the approach works ideally for opal and colloidal photonic crystals with a defined PBG, the IO structure is not simply a refractive-index contrast-reversed structure. This consideration becomes relevant for calculated IO pore diameters in Fig. 4 (d). Shown in black squares, are the calculated pore diameters found from the typical (111) Bragg-Snell analysis, with $d_{111} = \sqrt{\frac{2}{3}}D$. The grey shaded region represents one standard deviation about the SEM-calculated mean that was shown in Fig. 1 (i). None of the (111) calculated pore diameters fall within this range, most values ~100 nm from the measured mean pore size. This presents a large discrepancy between theoretical and experimental observations for the case of the TiO_2 IO pore sizes and its true structure. Other attempts to optically characterize the structural properties of inverse opals, prepared from calcination of an infilled opal template, have reported similar issues, with many attributing this to a very large degree of shrinkage in pore size from the initial opal template [40,62-64]. The change in pore diameter from the starting sphere size from our analyses confirm that reasoning is likely not the case.

Based on the opal spectra, and a detailed angle-resolved analysis of the corresponding TiO_2 IO spectra, we present two alternative approaches that predict both the correct actual pore size and the correct effective refractive index. The first approach investigates possible alternative planes of interaction and forces the use of a forbidden reflection from Bragg selection rules for an FCC system, while the second resolves the true structure of the IO whose PBG spectral analysis yields the correct IO structural parameters. Shown as red circles, are the calculated pore diameters predicted for optical transmission involving a band gap with the (-211) plane in an FCC structure. A potential interaction with a (-211) plane would yield $d_{211} = \frac{1}{\sqrt{3}}D$. Pore diameters calculated from this method are well within one standard deviation of the SEM calculated mean, with many data points very close to calculated mean value (shown as a solid black line). A schematic representation of light interacting with a (-211) plane is shown in Fig. 5(a,b).

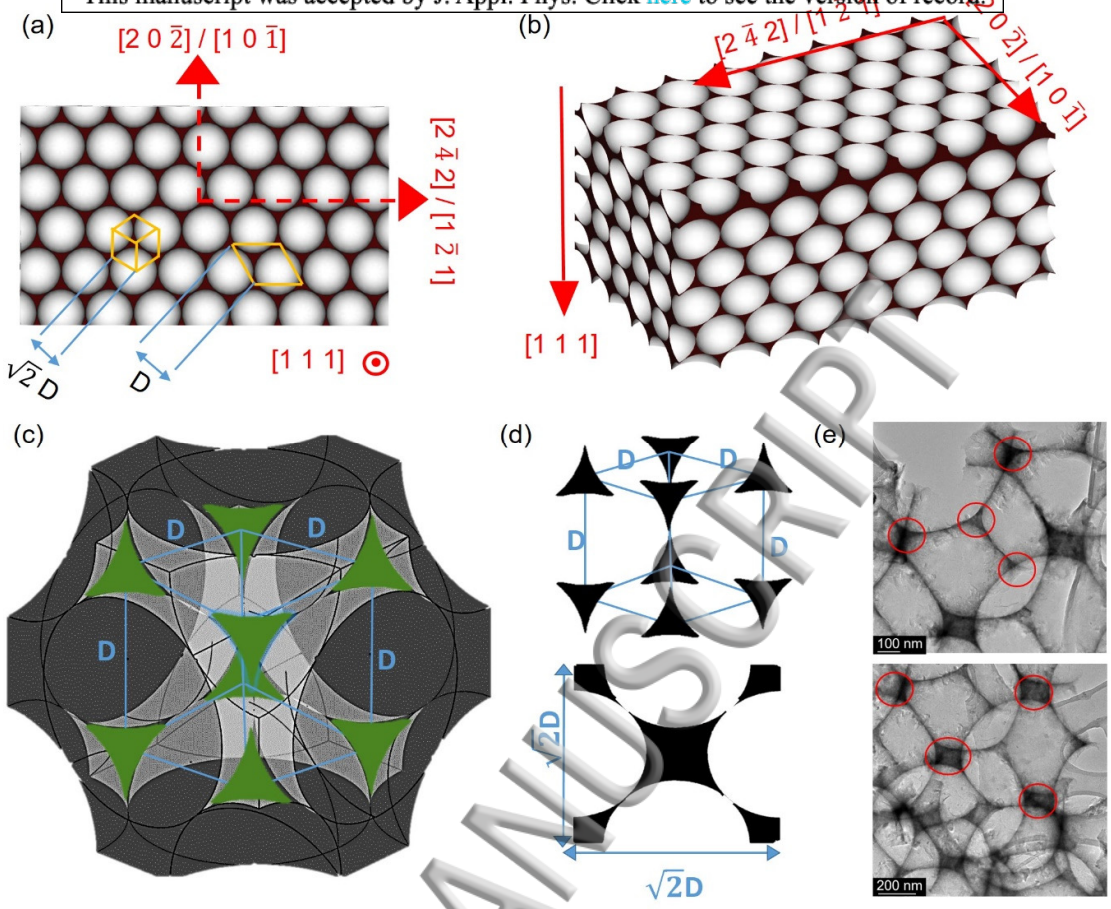

Figure 5. Schematic diagrams showing the directions of various {hkl} planes in an inverse opal structure from (a) plan view and (b) isometric view. Unit cells are marked on (a) to delineate the infilled tetrahedral voids of an FCC structure as an IO compared to an IO defined by the packing of the pore centroids. (c) Interconnected tetrahedral sites (shown in green) in an FCC unit cell showing a reduced unit cell parameter of length *D*. (d) Unit cells formed from interstitial tetrahedral sites with reduced unit cell parameter of length *D* and from interstitial octahedral sites with standard unit cell parameter of length $\sqrt{2}$ *D*. (e) Transmission electron microscopy (TEM) images of TiO_2 inverse opals highlighting the interstitial tetrahedral and octahedral sites of material.

As shown in Fig. 5, the (-211) and (-101) planes are oriented at 90 ° to the (111) plane typically used in Bragg-Snell analysis. For the D_{500} TiO_2 IO with incident angle varied about normal incidence, a strong linear correlation with Eqn 3 is found. As a result, proposed alternative planes of interaction were limited to those parallel or perpendicular to the (111) plane. For two planes in a cubic system, of Miller indices ($h_1k_1l_1$) and ($h_2k_2l_2$), the angle between the planes (φ) can be calculated from:

$$\varphi = Cos^{-1}\left(\frac{h_1h_2 + k_1k_2 + l_1l_2}{\left(\sqrt{h_1^2 + k_1^2 + l_1^2}\right)\left(\sqrt{h_2^2 + k_2^2 + l_2^2}\right)}\right) \qquad (6)$$

From Eqn 6, the low index planes perpendicular to the (111) plane include the (-211) and (-101) planes, with the associated interplanar spacing of the perpendicular (-211) plane providing a good fit for experimental observations and the Bragg-Snell law. The possible parallel planes (222), (333) etc. greatly overestimate IO pore sizes compared to measured results. However, the (-211) plane is not a permitted reflection (and hence transmission interaction) by Bragg selection rules for an FCC structure, which must have all odd or all even {hkl} combinations of Miller indices. It is possible that the selection rules for inverse opal nanomaterials are not as restrictive, with some reports of nanostructured materials presenting forbidden reflections in their electron diffraction patterns [65,66] – the analogy is assumed here for a photonic band structure. For inverted opal systems, the interconnected scaffold of a once ordered sphere stack may not replicate the ideal FCC structure completely, possibly resulting in less rigid selection rules. While plausible, we do not propose these possibilities allow forbidden reflections to be considered in the optical response of IOs in spite of yielding correct values. Planes perpendicular to the (111) plane would also have their associated normal at 90° to the incident light source. Analysis was performed assuming that the angle between the normal and light source was fixed at 0°. It is questionable whether or not these perpendicular planes could interact with light at this angle, in spite of the geometric fit with the data for the (-211) plane. Nevertheless, treating the angle-resolved band gap experimental data with an interplanar spacing of $d_{hkl} = \frac{1}{\sqrt{3}} D$, as per the (-211) plane, yields TiO_2 pore sizes in an IO that agree with measurements from SEM imaging.

A second approach to explain the large discrepancy between the theoretical predictions of the Bragg-Snell law and the experimentally reported TiO_2 IO pore sizes, comes from considering light interactions with the interstitial void sites of the opal template. In an FCC sphere packing arrangement, octahedral and tetrahedral spaces exist between the solid spheres of the opal, arising from the ABC stacking of each single layer of spheres. It is these voids in the opal structure that are infilled with precursor, prior to calcination. Post calcination, these occupied interstitial sites comprise the interconnected inverse opal network. A schematic representation of these interstitial spaces can be seen depicted in Fig. 5 (c) and (d). The tetrahedral spaces for the standard FCC unit cell are highlighted in Fig. 5 (c) and (d), whereas Fig. 5 (d) shows the octahedral sites. There are eight tetrahedral and four octahedral sites in the unit cell for an FCC structure. The octahedral spaces form a unit cell identical to that of the parent sphere structure, with a unit cell length $a = \sqrt{2}\, D$. As shown in

Fig. 5 (c), the tetrahedral voids form a different unit cell of length $a = D$. The presence of the interstitial sites in the prepared TiO_2 IO is highlighted in the TEM images included in Fig. 5 (e) where the interstitial sites can be seen to be connected as described in Fig. 5 (c) and (d). It has been reported, that upon infiltration of the precursor into the opal template, the tetrahedral sites of the material are completely filled before the octahedral sites [67]. It has also been suggested that the theoretical maximum infiltration of the opal material (26%) is unlikely to be attained in the infiltration step, resulting in incompletely filled inverse opal structures ($\varphi < 26\%$) for the majority of synthesis methods [68]. This latter scenario is most common in infiltration methods that involve coating of the surface of each sphere in the opal, such as atomic layer deposition (ALD), where the curvature of the spherical surfaces leaves a small void between packed spheres. In our analysis, minute infill errors, if they occur, are not the cause of the large blue-shift due to Bragg-Snell interpretation used to explained the PBG and transmission from opal photonic crystals.

When considering a light interaction with an inverse opal structure, the analogy of air spheres surrounded by crystalline material is often applied. However, when just accounting for the crystalline material present, the structure can be seen as a connected scaffold of tetrahedral and octahedral sites. It is with this network of tetrahedral and octahedral material that the light is forced to interact with, regardless of the coincidence of the network of air spheres present in the structure.

We propose that any interactions with this type of structure may exhibit a preference for interacting with the periodicity present in the completely filled tetrahedral sites of the interconnected framework of material. In terms of a potential Bragg-Snell interaction with completely filled tetrahedral sites, the interplanar spacing for the typical (111) transmission interaction can be given as $d_{111} = \frac{1}{\sqrt{3}} D$ due to a change in the unit cell length. This value for the interplanar spacing yields identical results to those obtained for the 'forbidden' (-211) plane using the standard FCC unit cell length, $a = \sqrt{2}\, D$. In assuming a preference for interactions with material forming the periodic arrangement of tetrahedral sites in the IO structure, the discrepancy between the theory and experiment can be explained by a change in unit cell length of the inverse opal structure. This modification considers the connected tetrahedral sites of the parent FCC opal structure as the true structure that interacts with light in the inverse opal and that defines the pseudo photonic band gap for the structure (the IO material) rather than standard FCC unit cell length, which is the structure of the pores. Essentially, the

inverse opal structure and its optical signature, are not that of a purely inverse geometry for index contrast and periodicity. The structure of the voids between FCC packed sphere in the opal define the final inverse opal structure, and are accurately represented by the transmission spectra, shift of the PBG and the refractive index of the void filling material, and also the pore size left by removal of the original opal spheres. This approach can be applied to any inverse opal formed by infilling of a colloidal photonic crystal with FCC structure, and accurately predicts material parameters, angle-resolved diffraction behaviour via the location of band gaps, and defines the nature of the real periodic structure of an IO.

IV. Conclusions

The nature of light-matter interaction with inverse opal structures in general is distinctly different from an opal photonic crystal. While the structure has always been referred to as 'inverted', the actual periodic structure that defines a band gap for light propagation in an inverse opal is not a direct inverse of the opal. Rigorous analysis of both optical transmission spectra and structure of FCC packed, highly ordered opals and corresponding TiO_2 inverse opals demonstrates a significant inconsistency when the Bragg-Snell theory is used to explain and match the spectral response for both structures.

Optical analysis of transmission spectra for PS opals exhibit clear transmission minima which can be accurately assigned as the (111) transmission minima from Bragg-Snell theory. Experimentally extracted data for the diameter and refractive index of the PS spheres, from the standard Bragg-Snell analysis, shows excellent agreement with both quoted and measured parameters. The presence of Fabry-Perot resonances in the PS opal spectra indicate high quality and long-range order across the sample surface. Overall, the optical spectra of the PS opals strongly agree with the widely applied (111) Bragg-Snell law.

In stark contrast, the optical spectra of TiO_2 inverse opals were found to consistently and significantly deviate from the expectations of typical (111) Bragg-Snell analysis. Observed transmission minima consistently appear substantially blue-shifted from expected values, and calculated pores sizes severely underestimated the measured pore sizes from microscopy analyses. This trend persisted across many samples, all prepared from ordered PS opal templates whose angle-dependent spectral shift of the band gap, the sphere size and effective refractive index agreed with Bragg-Snell theory.

Optical transmission interactions with alternative planes were investigated as a possible explanation for the discrepancy between theoretical and experimental results. It was found that modelling the Bragg-Snell data with an interplanar spacing derived from the (-211) plane of the FCC lattice provides a more accurate estimate of IO pore size. However, while the interplanar spacing of the (-211) plane could provide a strong numerical match with experimental data, this approach forces the use of a forbidden reflection based on selection rules of FCC crystal symmetry, applied to the 'packing' of the pores in the IO. The normal from the (-211) plane is also oriented at 90° to the incident light, making it doubtful that the plane could interact with the incident light. Any planes parallel to the (111) plane, were found to greatly overestimate the IO pore sizes. Considering these factors, it is unlikely that the observed difference in experimental data from theoretical predictions could be attributed to interactions with other crystal planes.

A second approach to explaining the disparity between experimental data and theoretical predictions considers the skeleton of interconnected material that defines the inverse opal, from the filling of interstitial sites by TiO_2, or indeed any material in general. We proposed a preference for light interaction with the periodic arrangement of tetrahedral sites of material in resulting IO structure. This approach proposes a transmission interaction with a periodic structure comprising the completely filled tetrahedral sites in the material, effectively redefining the unit cell length of the structure and avoids a model where the physical periodic structure that diffracts light is based on pore arrangements rather than the arrangement of material. By treating the experimental data with this model, estimated pore sizes are accurate and consistent with those determined by SEM analysis. In comparison to results obtained from the (-211) plane model, this approach yields identical results, but uses a realistic structure of the inverse opal material directly, rather than a forbidden reflection and associated unit cell based on the parent opal template structure. Regardless of the correct interpretation of the possible underlying structure that defines the PBG and the diffraction, changing the interplanar spacing from $d_{111} = \sqrt{\frac{2}{3}}\,D$ to $\mathrm{d} = \frac{1}{\sqrt{3}}\,D$ was found to more accurately model the optical transmission spectra obtained for the TiO_2 inverse opals, and we posit that this consideration for the structure of an inverse opal is generally application to all inverse opals fashioned from an FCC opal with a fixed sphere size D, at least where $D/\lambda_{PBG} < 1$.

V. Supplementary Material

Electron microscopy of TiO_2 inverse opals and tilted cross-sections, and a typical image showing how pore diameter distributions were obtained from direct imaging are provided. Optical images of TiO_2 IO samples are also shown. A summary analysis of the angle-resolved optical spectra of IOs according to Bragg-Snell theory is also provided.

Acknowledgements

A.L. acknowledges support from the Irish Research Council Government of Ireland Postgraduate Scholarship under award no. GOIPG/2016/946. This work was supported by Science Foundation Ireland by an SFI Technology Innovation and Development Awards under contract no. 13/TIDA/E2761 and 15/TIDA/2893. This publication has also emanated from research supported in part by a research grant from SFI under Grant Number 14/IA/2581.

References

[1] E. Yablonovitch, Inhibited spontaneous emission in solid-state physics and electronics, Phys. Rev. Lett. **58**, 2059 (1987).
[2] S. John, Strong localization of photons in certain disordered dielectric superlattices, Phys. Rev. Lett. **58**, 2486 (1987).
[3] C. O'Dwyer, Color-coded batteries – Electro-photonic inverse opal materials for enhanced electrochemical energy storage and optically encoded diagnostics, Adv. Mater. **28**, 5681 (2016).
[4] J. F. Galisteo-López, E. Palacios-Lidón, E. Castillo-Martínez, and C. López, Optical study of the pseudogap in thickness and orientation controlled artificial opals, Phys. Rev. B **68**, 115109 (2003).
[5] K. Busch and S. John, Liquid-crystal photonic-band-gap materials: The tunable electromagnetic vacuum, Phys. Rev. Lett. **83**, 967 (1999).
[6] M. Lanata, M. Cherchi, A. Zappettini, S. M. Pietralunga, and M. Martinelli, Titania inverse opals for infrared optical applications, Opt. Mater. **17**, 11 (2001).
[7] K. R. Phillips, N. Vogel, Y. Hu, M. Kolle, C. C. Perry, and J. Aizenberg, Tunable anisotropy in inverse opals and emerging optical properties, Chem. Mater. **26**, 1622 (2014).
[8] E. Armstrong and C. O'Dwyer, Artificial opal photonic crystals and inverse opal structures - Fundamentals and applications from optics to energy storage, J. Mater. Chem. C **3**, 6109 (2015).
[9] G. Collins, E. Armstrong, D. McNulty, S. O'Hanlon, H. Geaney, and C. O'Dwyer, 2D and 3D photonic crystal materials for photocatalysis and electrochemical energy storage and conversion, Sci. Tech. Adv. Mater. **17**, 563 (2016).
[10] A. Stein, Batteries take charge, Nat. Nanotechnol. **6**, 262 (2011).
[11] Y. S. Zhang, C. Zhu, and Y. Xia, Inverse opal scaffolds and their biomedical applications, Adv. Mater. **29**, 1701115 (2017).
[12] S. Kim, A. N. Mitropoulos, J. D. Spitzberg, D. L. Kaplan, and F. G. Omenetto, Silk protein based hybrid photonic-plasmonic crystal, Opt. Express **21**, 8897 (2013).
[13] K. Busch and S. John, Photonic band gap formation in certain self-organizing systems, Phys. Rev. E **58**, 3896 (1998).
[14] X. Chen and S. S. Mao, Titanium dioxide nanomaterials: Synthesis, properties, modifications and applications, Chem. Rev. **107**, 2891 (2007).
[15] J. I. L. Chen, E. Loso, N. Ebrahim, and G. A. Ozin, Synergy of slow photon and chemically amplified photochemistry in platinum nanocluster-loaded inverse titania opals, J. Am. Chem. Soc. **130**, 5420 (2008).

[16] E. S. Thiele and R. H. French, Light-scattering properties of representative, morphological rutile titania particles studied using a finite-element method, J. Am. Ceram. Soc. **81**, 469 (1998).
[17] L. Mishchenko, B. Hatton, M. Kolle, and J. Aizenberg, Patterning hierarchy in direct and inverse opal crystals, Small **8**, 1904 (2012).
[18] D. McNulty, H. Geaney, and C. O'Dwyer, Carbon-coated honeycomb Ni-Mn-Co-O inverse opal: A high capacity ternary transition metal oxide anode for Li-ion batteries, Sci. Rep. **7**, 42263 (2017).
[19] A. Mihi, M. Ocaña, and H. Míguez, Oriented colloidal-crystal thin films by spin-coating microspheres dispersed in volatile media, Adv. Mater. **18**, 2244 (2006).
[20] C. Deleuze, B. Sarrat, F. Ehrenfeld, S. Perquis, C. Derail, and L. Billon, Photonic properties of hybrid colloidal crystals fabricated by a rapid dip-coating process, Phys. Chem. Chem. Phys. **13**, 10681 (2011).
[21] I. Yamaguchi, M. Watanabe, T. Shinagawa, M. Chigane, M. Inaba, A. Tasaka, and M. Izaki, Preparation of core/shell and hollow nanostructures of cerium oxide by electrodeposition on a polystyrene sphere template, ACS Appl. Mater. Interfaces **1**, 1070 (2009).
[22] S. Reculusa and S. Ravaine, Synthesis of colloidal crystals of controllable thickness through the Langmuir−Blodgett technique, Chem. Mater. **15**, 598 (2003).
[23] A. S. Dimitrov and K. Nagayama, Continuous convective assembling of fine particles into two-dimensional arrays on solid surfaces, Langmuir **12**, 1303 (1996).
[24] E. A. Gaulding *et al.*, Fabrication and optical characterization of polystyrene opal templates for the synthesis of scalable, nanoporous (photo)electrocatalytic materials by electrodeposition, J. Mater. Chem. A **5**, 11601 (2017).
[25] J. D. Joannopoulos, P. R. Villeneuve, and S. Fan, Photonic crystals: Putting a new twist on light, Nature **386**, 143 (1997).
[26] C. López, Materials aspects of photonic crystals, Adv. Mater. **15**, 1679 (2003).
[27] D. Van Gough, A. T. Juhl, and P. V. Braun, Programming structure into 3D nanomaterials, Mater. Today **12**, 28 (2009).
[28] K. R. Phillips, G. T. England, S. Sunny, E. Shirman, T. Shirman, N. Vogel, and J. Aizenberg, A colloidoscope of colloid-based porous materials and their uses, Chem. Soc. Rev. **45**, 281 (2016).
[29] G. Collins, M. Blömker, M. Osiak, J. D. Holmes, M. Bredol, and C. O'Dwyer, Three-dimensionally ordered hierarchically porous tin dioxide inverse opals and immobilization of palladium nanoparticles for catalytic applications, Chem. Mater. **25**, 4312 (2013).
[30] A. Vu, Y. Qian, and A. Stein, Porous electrode materials for lithium-ion batteries – How to prepare them and what makes them special, Adv. Energy. Mater. **2**, 1056 (2012).
[31] D. McNulty, E. Carroll, and C. O'Dwyer, Rutile TiO2 inverse opal anodes for Li-ion batteries with long cycle life, high-rate capability, and high structural stability, Adv. Energy. Mater. **7**, 1602291 (2017).
[32] H. Zhang, X. Yu, and P. V. Braun, Three-dimensional bicontinuous ultrafast-charge and -discharge bulk battery electrodes, Nat. Nanotechnol. **6**, 277 (2011).
[33] L. K. Teh, C. C. Wong, H. Y. Yang, S. P. Lau, and S. F. Yu, Lasing in electrodeposited ZnO inverse opal, Appl. Phys. Lett. **91**, 161116 (2007).
[34] D. Zhang, S. Chen, M. Jiang, and L. Ye, Optimization of lasing in an inverted-opal titania photonic crystal cavity as an organic solid-state dye-doped laser, Appl. Opt **53**, 7624 (2014).
[35] J. Martorell, R. Vilaseca, and R. Corbalán, Scattering of second-harmonic light from small spherical particles ordered in a crystalline lattice, Phys. Rev. A **55**, 4520 (1997).
[36] A. A. Fedyanin, O. A. Aktsipetrov, D. A. Kurdyukov, V. G. Golubev, and M. Inoue, Nonlinear diffraction and second-harmonic generation enhancement in silicon-opal photonic crystals, Appl. Phys. Lett. **87**, 151111 (2005).
[37] P. P. Markowicz, H. Tiryaki, H. Pudavar, P. N. Prasad, N. N. Lepeshkin, and R. W. Boyd, Dramatic Enhancement of Third-Harmonic Generation in Three-Dimensional Photonic Crystals, Phys. Rev. Lett. **92**, 083903 (2004).
[38] O. Y. Stanislav, I. Z. Kirill, A. G. Evgeny, V. Y. Egor, K. Z. Arsen, M. M. Vladimir, A. E. Gennadi, and S. G. Vladimir, Enhanced third-harmonic generation in photonic crystals at band-gap pumping, J. Phys. D **50**, 055105 (2017).
[39] J.-Q. Wang, Y.-Y. Wu, S.-S. Yuan, M. Zhang, and X.-B. Chen, Preparation and optical properties of tin dioxide inverse opal film, Rare Met. (2015).
[40] V. Jovic, T. Söhnel, J. Metson, and G. Waterhouse, in *Matter and Materials Meeting* (2011), p. 26.
[41] J. S. King, E. Graugnard, and C. J. Summers, TiO2 inverse opals fabricated using low-temperature atomic layer deposition, Adv. Mater. **17**, 1010 (2005).
[42] C. Cheng, S. K. Karuturi, L. Liu, J. Liu, H. Li, L. T. Su, A. I. Y. Tok, and H. J. Fan, Quantum-Dot-Sensitized TiO2 Inverse Opals for Photoelectrochemical Hydrogen Generation, Small **8**, 37 (2012).
[43] A. Mills and M. Crow, A study of factors that change the wettability of titania films, Int. J. Photoenergy **2008** (2008).
[44] E. Pavarini, L. C. Andreani, C. Soci, M. Galli, F. Marabelli, and D. Comoretto, Band structure and optical properties of opal photonic crystals, Phys. Rev. B **72**, 045102 (2005).

[45] J. Fang, Y. Xuan, and Q. Li, Preparation of polystyrene spheres in different particle sizes and assembly of the PS colloidal crystals, Sci. China. Technol. Sci. **53**, 3088 (2010).
[46] D. S. Raimundo, F. J. Fernandez, and W. J. Salcedo, Self-assembled polystyrene micro-spheres applied for photonic crystals and templates fabrication, J. Integrated. Circuits. Syst. **1**, 39 (2006).
[47] H. Zhang, R.-g. Duan, F. Li, Q. Tang, and W.-c. Li, Microscopy evidence of the face-centered cubic arrangement of monodisperse polystyrene nanospheres, Mater. Des. **28**, 1045 (2007).
[48] Y. Xie, R. Xing, Q. Li, L. Xu, and H. Song, Three-dimensional ordered ZnO–CuO inverse opals toward low concentration acetone detection for exhaled breath sensing, Sens. Actuator B-Chem. **211**, 255 (2015).
[49] D. Reyes-Coronado, G. Rodríguez-Gattorno, M. E. Espinosa-Pesqueira, C. Cab, R. d. Coss, and G. Oskam, Phase-pure TiO2 nanoparticles: anatase, brookite and rutile, Nanotechnology **19**, 145605 (2008).
[50] B. K. Mutuma, G. N. Shao, W. D. Kim, and H. T. Kim, Sol–gel synthesis of mesoporous anatase–brookite and anatase–brookite–rutile TiO2 nanoparticles and their photocatalytic properties, J. Colloid Interface Sci. **442**, 1 (2015).
[51] M. G. Brik, Antic, Zcaron, M. eljka, K. Vukovic, and M. D. Dramicanin, Judd-Ofelt analysis of Eu3+ emission in TiO2 anatase nanoparticles, Mater. Trans. **56**, 1416 (2015).
[52] F. Tian, Y. Zhang, J. Zhang, and C. Pan, Raman spectroscopy: A new approach to measure the percentage of anatase TiO2 exposed (001) facets, J. Phys. Chem. C **116**, 7515 (2012).
[53] Y. Nishijima, K. Ueno, S. Juodkazis, V. Mizeikis, H. Misawa, T. Tanimura, and K. Maeda, Inverse silica opal photonic crystals for optical sensing applications, Opt. Express **15**, 12979 (2007).
[54] K. Sumioka, H. Kayashima, and T. Tsutsui, Tuning the optical properties of inverse opal photonic crystals by deformation, Adv. Mater. **14**, 1284 (2002).
[55] J. C. Hong, J. H. Park, C. Chun, and D. Y. Kim, Photoinduced tuning of optical stop bands in azopolymer based inverse opal photonic crystals, Adv. Funct. Mater. **17**, 2462 (2007).
[56] J. Wang, C. Zhou, L. Su, X. Ji, X. Chen, and M. Zhang, Preparation of inverse opal cerium dioxide for optical properties research, Mater. Lett. **158**, 123 (2015).
[57] S. H. Jones, M. D. King, and A. D. Ward, Determining the unique refractive index properties of solid polystyrene aerosol using broadband Mie scattering from optically trapped beads, Phys. Chem. Chem. Phys. **15**, 20735 (2013).
[58] S. G. Romanov, M. Bardosova, I. M. Povey, M. E. Pemble, and C. M. S. Torres, Understanding of transmission in the range of high-order photonic bands in thin opal film, Appl. Phys. Lett. **92**, 191106 (2008).
[59] T. Maka, D. Chigrin, S. Romanov, and C. Torres, Three dimensional photonic crystals in the visible regime, Prog. Electromagn. Res. **41**, 307 (2003).
[60] K. S. Napolskii *et al.*, Fabrication of artificial opals by electric-field-assisted vertical deposition, Langmuir **26**, 2346 (2010).
[61] E. Graugnard, V. Chawla, D. Lorang, and C. J. Summers, High filling fraction gallium phosphide inverse opals by atomic layer deposition, Appl. Phys. Lett. **89**, 211102 (2006).
[62] T. K. Rahul and N. Sandhyarani, Nitrogen-fluorine co-doped titania inverse opals for enhanced solar light driven photocatalysis, Nanoscale **7**, 18259 (2015).
[63] Y. Li, F. Piret, T. Léonard, and B.-L. Su, Rutile TiO2 inverse opal with photonic bandgap in the UV–visible range, J. Colloid Interface Sci. **348**, 43 (2010).
[64] S. Lusi, C. Bin, K. Kyoji, S. Okihiro, and K. Toshikuni, Fabrication of Inverse Opal TiO 2 Waveguide Structure, Jpn. J. Appl. Phys. **47**, 1208 (2008).
[65] D. C. Bell, Y. Wu, C. J. Barrelet, S. Gradečak, J. Xiang, B. P. Timko, and C. M. Lieber, Imaging and analysis of nanowires, Microsc. Res. Tech. **64**, 373 (2004).
[66] J. Reyes-Gasga, A. Gómez-Rodríguez, X. Gao, and M. José-Yacamán, On the interpretation of the forbidden spots observed in the electron diffraction patterns of flat Au triangular nanoparticles, Ultramicroscopy **108**, 929 (2008).
[67] D. Gaillot, T. Yamashita, and C. J. Summers, Photonic band gaps in highly conformal inverse-opal based photonic crystals, Phys. Rev. B **72**, 205109 (2005).
[68] D. P. Gaillot and C. J. Summers, Photonic band gaps in non-close-packed inverse opals, J. Appl. Phys. **100**, 113118 (2006).

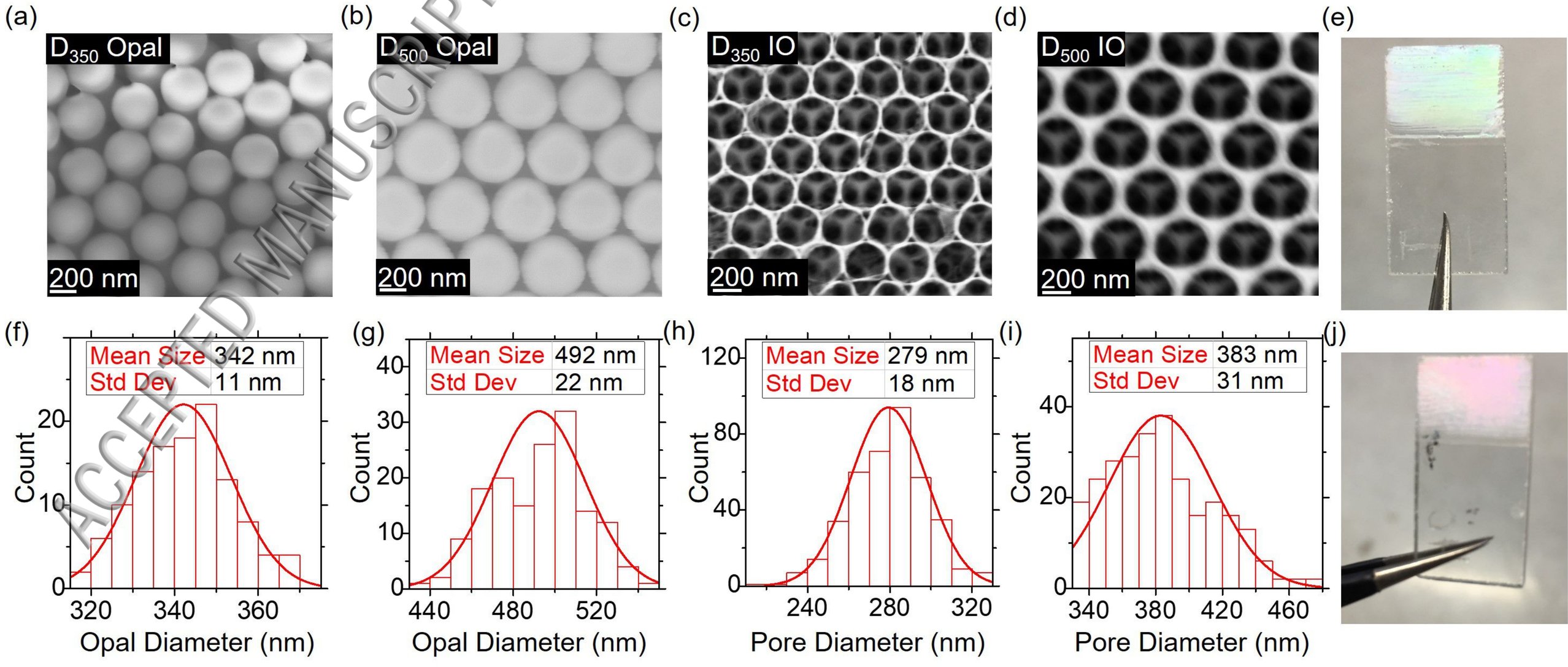

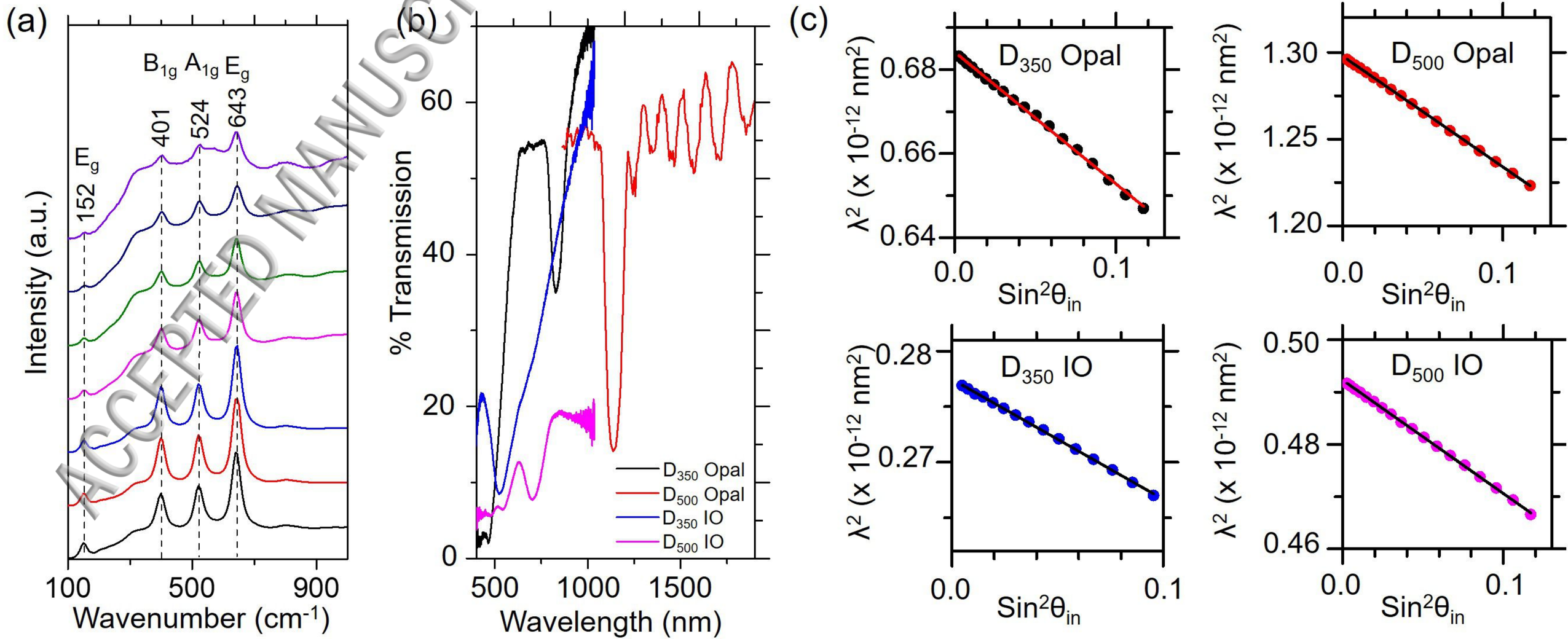

(a)

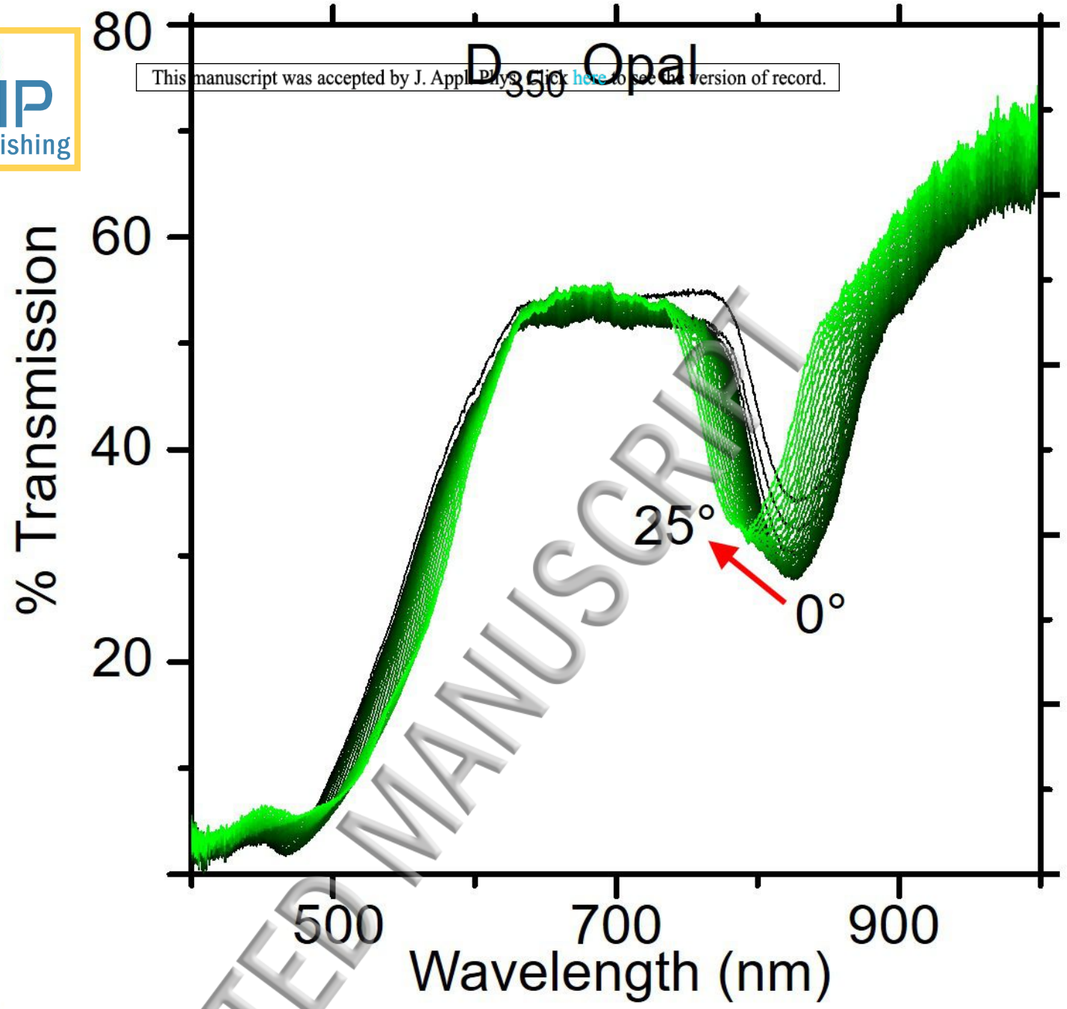

(b)

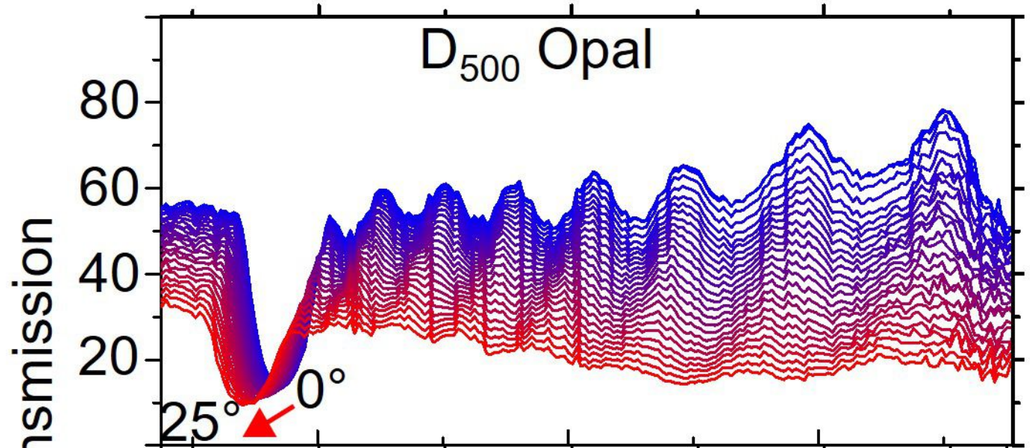

(c)

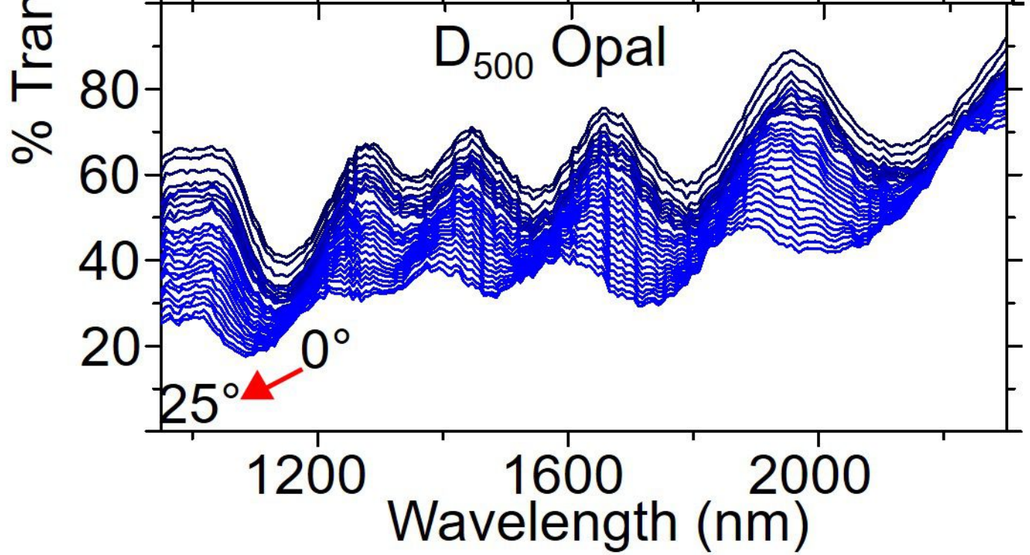

(d)

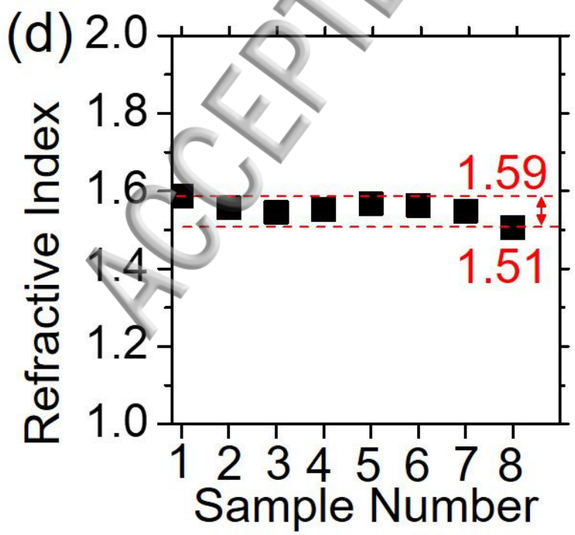

(e)

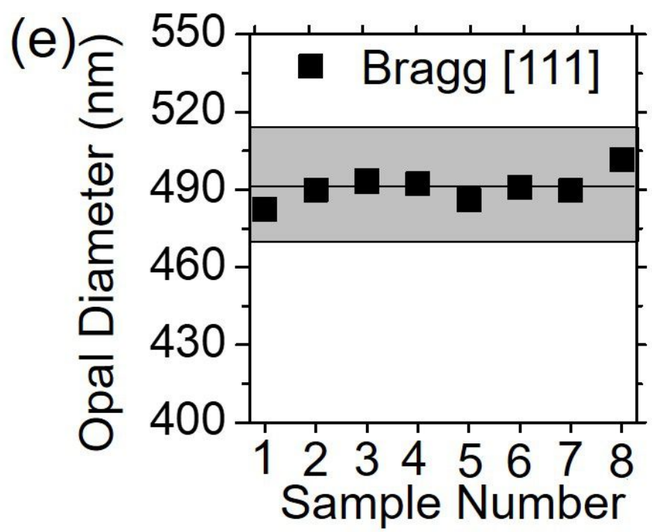

(f)

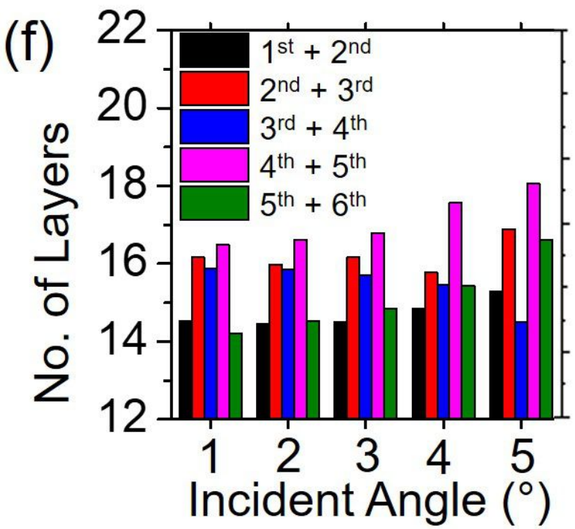

(g)

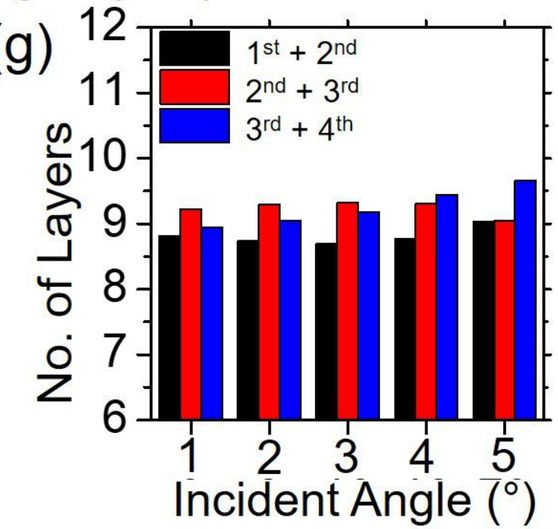

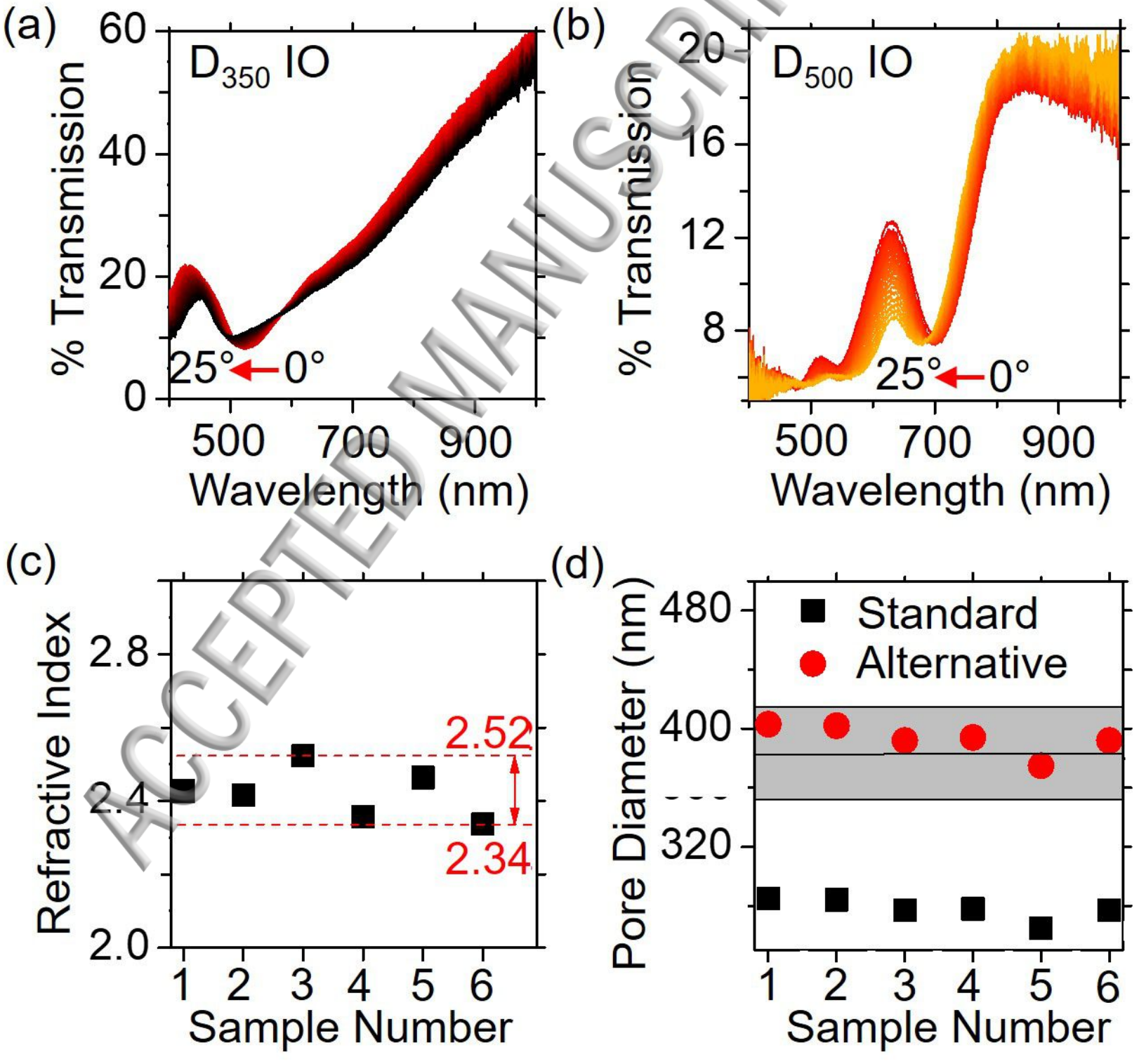

(a)

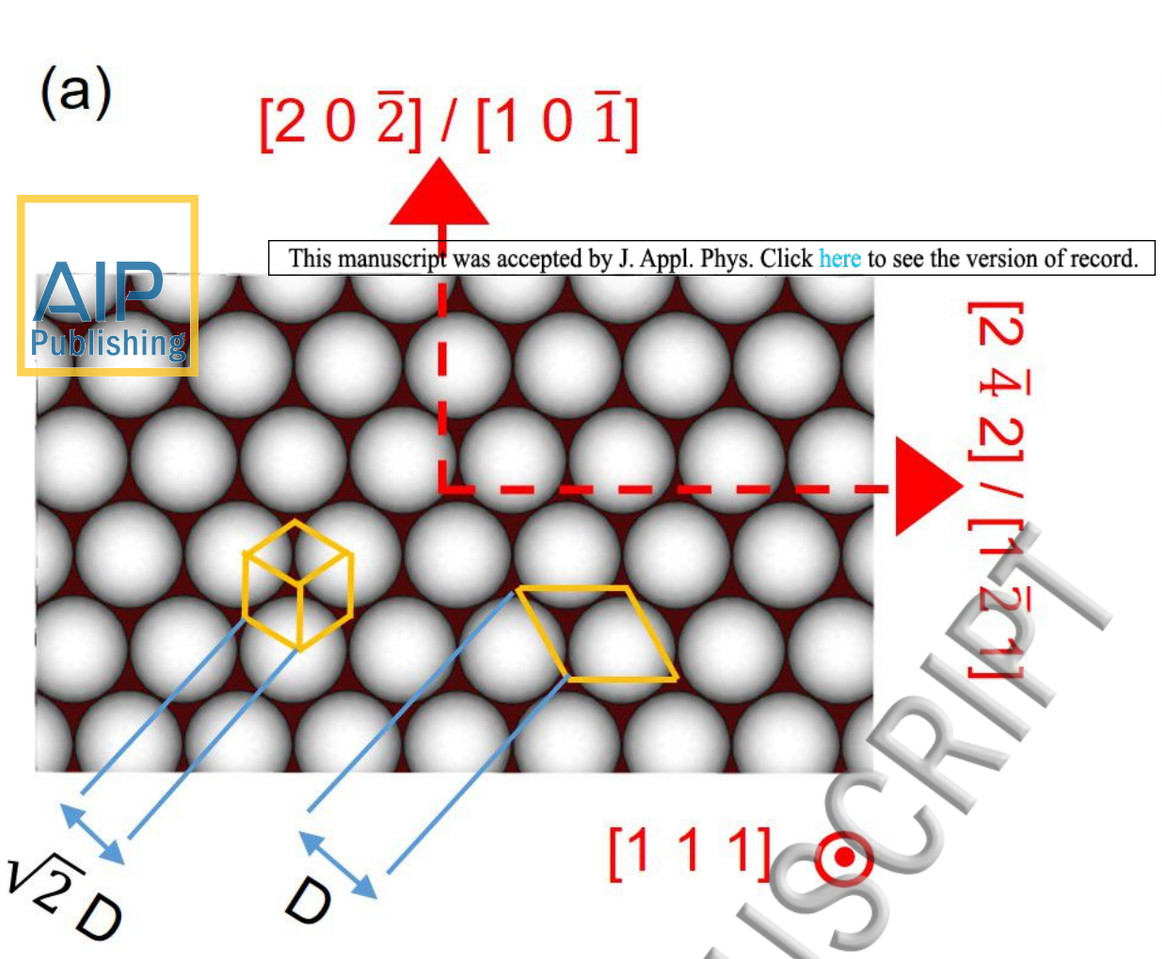

(b)

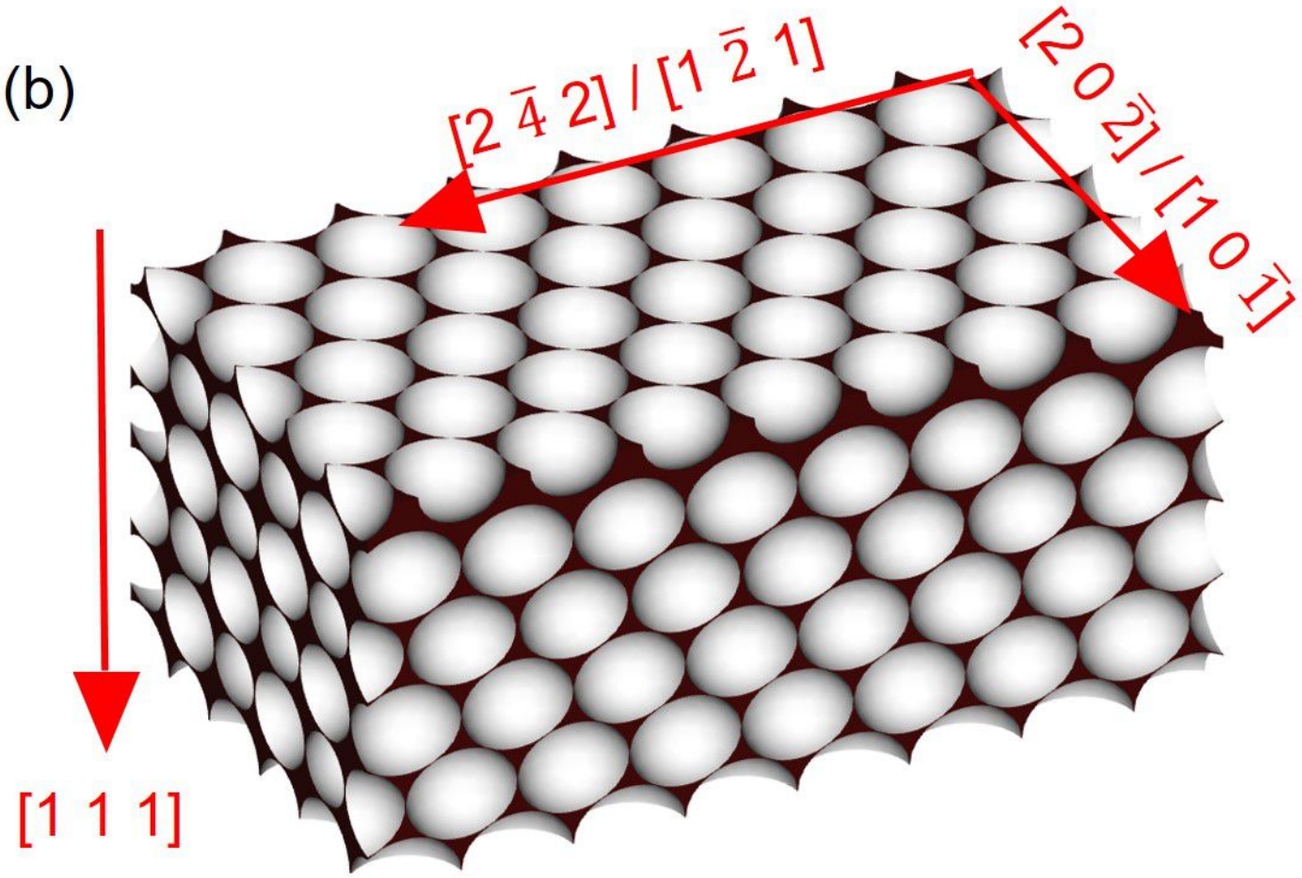

(c)

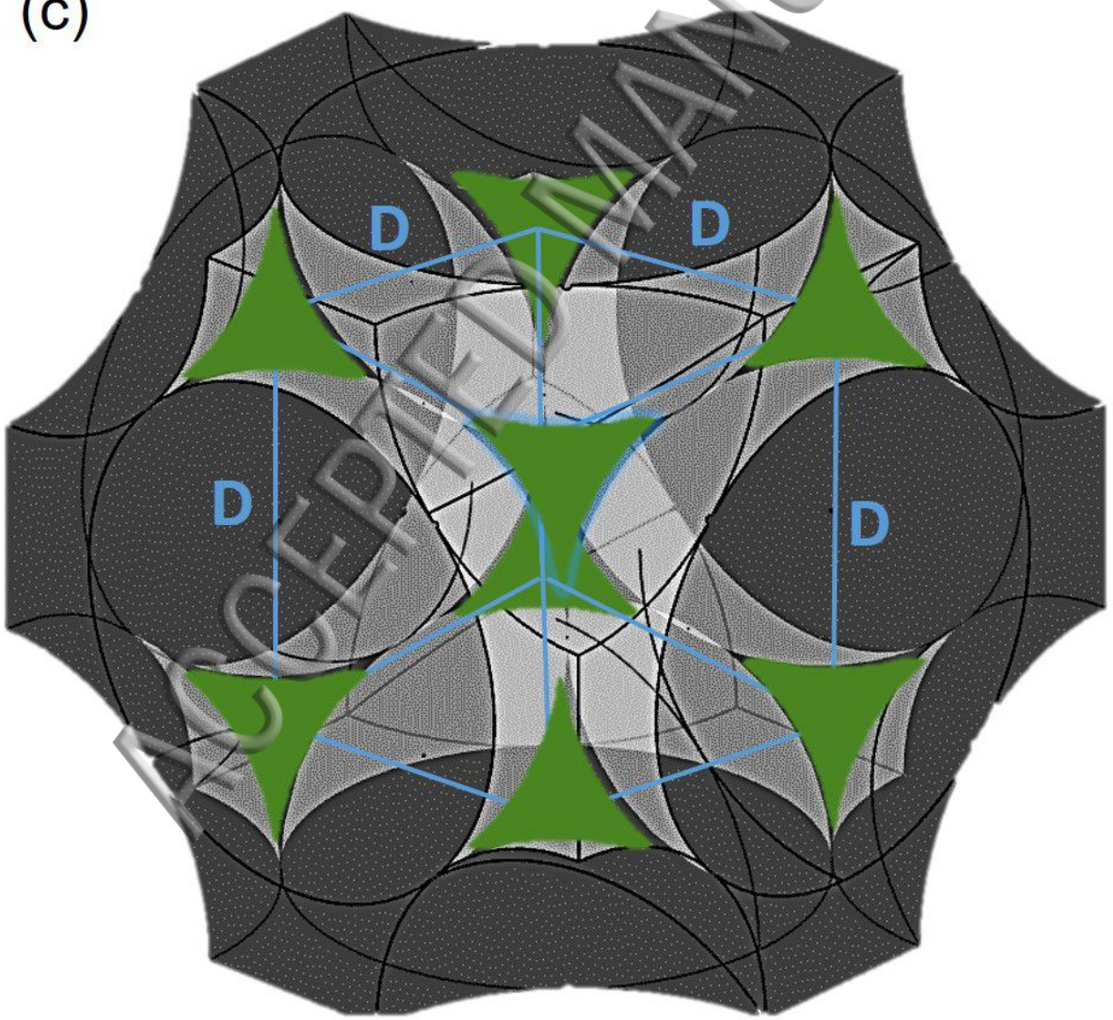

(d)

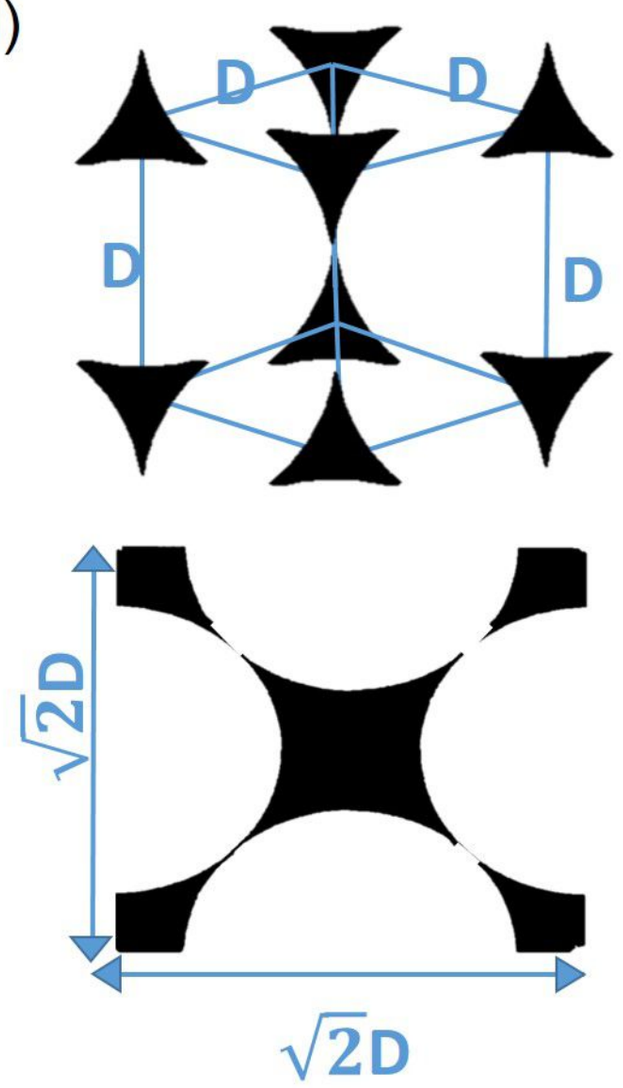

(e)